Supporting Information:

Plasma-Catalytic Partial Oxidation of Methane on Pt(111): a Microkinetic Study of the Role of Different Plasma Species

Björn Loenders*, Yannick Engelmann and Annemie Bogaerts

Research group PLASMANT, Department of Chemistry, University of Antwerp,

Universiteitsplein 1, B-2610 Wilrijk-Antwerp, Belgium

*E-mail: bjorn.loenders@uantwerpen.be

1. The chemistry set and corresponding thermodynamic data

The different reactions included in the model, for both thermal and plasma catalysis, are listed in Table S1, together with the corresponding activation and reaction enthalpies ($\Delta H^{\ddagger}$ and ΔH, resp.). The implementation of the entropies is described in the main paper.

Table S1. List of reactions included in the model, for both thermal and plasma catalysis (plasma reactions listed separately), with the corresponding activation and reaction enthalpies on Pt(111) and their associated references.[a]

N°	Dissociative adsorption / Associative desorption	$\Delta H^{\ddagger}$ (eV)	Ref.	ΔH (eV)	Ref.
1	$CH_4(g) + 2* \rightleftharpoons CH_3* + H*$	0.63	1	-0.28	1
2	$O_2(g) + 2* \rightleftharpoons 2O*$	-0.07[b]	2	-1.89[b]	2
3	$H_2(g) + 2* \rightleftharpoons 2H*$	0.19	1	-0.67	1
4	$CH_3CH_3(g) + 2* \rightleftharpoons 2CH_3*$	1.09[c]	3	-0.30[d]	1
5	$HCOOH(g) + 2* \rightleftharpoons H* + COOH*$	0.22	4	-0.84	4
6	$HCOOH(g) + 2* \rightleftharpoons HCOO* + H*$	0.25[e]	4	-0.45[f]	
N°	**Molecular adsorption / desorption**	**$\Delta H^{\ddagger}$ (eV)[g]**	**Ref.**	**ΔH (eV)**	**Ref.**
7	$CH_2CH_2(g) + * \rightleftharpoons CH_2CH_2*$	0.00	-	-1.51	1
8	$CHCH(g) + * \rightleftharpoons CHCH*$	0.00	-	-2.87	1
9	$CO(g) + * \rightleftharpoons CO*$	0.00	-	-1.41	5
10	$CO_2(g) + * \rightleftharpoons CO_2*$	0.00	-	-0.03	6
11	$H_2O(g) + * \rightleftharpoons H_2O*$	0.00	-	-0.22	5
12	$CH_3OH(g) + * \rightleftharpoons CH_3OH*$	0.00	-	-0.34	7
13	$CH_2O(g) + * \rightleftharpoons CH_2O*$	0.00	-	-0.50	8

N°	Eley-Rideal reactions	ΔH‡ (eV)	Ref.	ΔH (eV)	Ref.
14	$CH_4(g) + OH^* + * \rightleftharpoons CH_3^* + H_2O^*$	0.50	7	-0.86	7
15	$CH_4(g) + O^* + * \rightleftharpoons CH_3^* + OH^*$	1.28	7	-0.13	7
N°	**Langmuir-Hinshelwood reactions**	**ΔH‡ (eV)**	**Ref.**	**ΔH (eV)**	**Ref.**
16	$CH_3^* + * \rightleftharpoons CH_2^* + H^*$	0.83	1	0.07	1
17	$CH_2^* + * \rightleftharpoons CH^* + H^*$	0.17	1	-0.65	1
18	$CH^* + * \rightleftharpoons C^* + H^*$	1.29	1	0.47	1
19	$CH_3^* + O^* \rightleftharpoons CH_2^* + OH^*$	1.62	7	0.22	7
20	$CH_2^* + O^* \rightleftharpoons CH^* + OH^*$	1.44	7	-0.50	7
21	$CH^* + O^* \rightleftharpoons C^* + OH^*$	2.13	7	0.62	7
22	$CH_3^* + OH^* \rightleftharpoons CH_2^* + H_2O^*$	1.07	7	-0.51	7
23	$CH_2^* + OH^* \rightleftharpoons CH^* + H_2O^*$	0.31	7	-1.23[h]	7
24	$CH^* + OH^* \rightleftharpoons C^* + H_2O^*$	0.77	7	-0.11[h]	7
25	$CH_3^* + O^* \rightleftharpoons CH_3O^* + *$	2.04	7	0.34	7
26	$CH_2^* + O^* \rightleftharpoons CH_2O^* + *$	2.18	7	-0.29	7
27	$CH^* + O^* \rightleftharpoons CHO^* + *$	1.69	7	-0.42	7
28	$C^* + O^* \rightleftharpoons CO^* + *$	1.92	7	-1.84	7
29	$CH_3^* + OH^* \rightleftharpoons CH_3OH^* + *$	2.02	7	-0.18	7
30	$CH_2^* + OH^* \rightleftharpoons CH_2OH^* + *$	1.05	7	-0.75	7
31	$CH^* + OH^* \rightleftharpoons CHOH^* + *$	1.17	7	-0.42	7
32	$C^* + OH^* \rightleftharpoons COH^* + *$	1.08	7	-1.47	7
33	$CH_3OH^* + * \rightleftharpoons CH_2OH^* + H^*$	0.77	7	-0.50[h]	7
34	$CH_2OH^* + * \rightleftharpoons CHOH^* + H^*$	0.63	7	-0.32[h]	7
35	$CHOH^* + * \rightleftharpoons COH^* + H^*$	0.62	7	-0.58[h]	7
36	$CH_3OH^* + * \rightleftharpoons CH_3O^* + H^*$	0.80	7	0.37[h]	7
37	$CH_2OH^* + * \rightleftharpoons CH_2O^* + H^*$	0.99	7	0.31[h]	7
38	$CHOH^* + * \rightleftharpoons CHO^* + H^*$	0.54	7	-0.15[h]	7
39	$COH^* + * \rightleftharpoons CO^* + H^*$	0.84	7	-0.52	7
40	$CH_3O^* + * \rightleftharpoons CH_2O^* + H^*$	0.24	7	-0.56[h]	7
41	$CH_2O^* + * \rightleftharpoons CHO^* + H^*$	0.14	7	-0.78[h]	7
42	$CHO^* + * \rightleftharpoons CO^* + H^*$	0.36	7	-0.95	7
43	$2CH_2^* \rightleftharpoons CH_2CH_2^* + *$	1.59	1	-0.63	1

44	2CH* ⇌ CHCH* + *	1.78	1	0.71	1
45	O* + H* ⇌ OH* + *	1.09	6	0.15	6
46	OH* + H* ⇌ H_2O* + *	0.20	6	-0.58[h]	6
47	OH* + OH* ⇌ H_2O* + H*	0.00	6	-0.73[h]	6
48	CO* + O* ⇌ CO_2* + *	1.07	6	0.14	6
49	C* + CO2* ⇌ CO* + CO*	0.00	9	-1.98[f]	
50	CO* + OH* ⇌ COOH* + *	0.46	6	-0.24	6
51	COOH* + * ⇌ CO_2* + H*	0.85	6	0.23[h]	6
52	COOH* + O* ⇌ CO_2* + OH*	0.47	6	0.38[h]	6
53	COOH* + OH* ⇌ CO_2* + H_2O*	0.10	6	-0.35	6
54	CHO* + O* ⇌ CHOO* + *	1.03	6	-0.65	6
55	HCOO* + * ⇌ CO_2* + H*	1.04	6	-0.16[h]	6
56	HCOO* + O* ⇌ CO_2* + OH*	1.74	6	-0.01[h]	6
57	HCOO* + OH* ⇌ CO_2* + H_2O*	1.01	6	-0.74	6
Specific plasma reactions					
N°	**Radical adsorption / desorption**	**$\Delta H^{\ddagger}$ (eV)[g]**	**Ref.**	**ΔH (eV)**	**Ref.**
58	CH_3(g) + * ⇌ CH_3*	0.00	-	-2.16	1
59	CH_2(g) + * ⇌ CH_2*	0.00	-	-4.12	1
60	CH(g) + * ⇌ CH*	0.00	-	-7.31	1
61	C(g) + * ⇌ C*	0.00	-	-7.05	1
62	O(g) + * ⇌ O*	0.00	-	-3.93	6
63	H(g) + * ⇌ H*	0.00	-	-2.74	6
64	OH(g) + * ⇌ OH*	0.00	-	-2.44	6
65	CH_3O(g) + * ⇌ CH_3O*	0.00	-	-1.43[i]	10
66	CHO(g) + * ⇌ CHO*	0.00	-	-2.66	6
67	OOH(g) + * ⇌ OOH*	0.00	-	-1.06	11
68	CH_3OO(g) + * ⇌ CH_3OO*	0.00	-	-1.06[j]	
69	COOH(g) + * ⇌ COOH* [k]	0.00	-	-2.59	6
70	HCOO(g) + * ⇌ HCOO* [k]	0.00	-	-2.42	6
N°	**Langmuir-Hinshelwood reactions**	**$\Delta H^{\ddagger}$ (eV)**	**Ref.**	**ΔH (eV)**	**Ref.**
71	OOH* + * ⇌ OH* + O*	0.14	11	-1.25	12
72	CH_3OO* + * ⇌ CH_3O* + O*	0.14[j]	-	-1.25[j]	-

N°	Eley-Rideal reactions[l]	$\Delta H^{\ddagger}$ (eV)[l]	Ref.	ΔH (eV)	Ref.
73	$CH_3(g) + O^* \rightleftharpoons CH_3O^*$	-	-	-1.82[f]	-
74	$H(g) + O^* \rightleftharpoons OH^*$	-	-	-2.59[f]	-
75	$O(g) + C^* \rightleftharpoons CO^*$	-	-	-5.77[f]	-

a. Empty surface sites are denoted by '*'. However, not all species adsorb on the same type of site. The '*' thus represents the fraction of the empty surface, rather than the fraction of a specific type of sites.

b. For convenience, the data for molecular adsorption of O_2 and dissociation of O_2*, reported in ref. 2, are combined in one dissociative adsorption reaction. Because the enthalpy barrier for dissociation is lower than the adsorption enthalpy, the resulting enthalpy of activation has a negative value. This is not a problem as long as the total Gibbs free energy barrier is positive, which is the case for all temperatures above 81 K. The reaction enthalpy is calculated as the sum of the reaction enthalpies of the adsorption of O_2 and the dissociation of O_2*.

c. Calculated using Brønsted-Evans-Polanyi relation for C-C cleavage from ref. 3.

d. The reaction enthalpy is calculated from the enthalpies of the other reactions reported in ref. 1.

e. Recalculated from the enthalpy of the reverse reaction from ref. 4 and the reaction enthalpy used in our model.

f. The reaction enthalpy is calculated based on those of other reactions included in the chemistry set to ensure thermodynamic consistency.

g. Molecular and radical adsorption processes are assumed to occur without enthalpy barrier.

h. The reaction enthalpies are changed by 0.01 eV to ensure thermodynamic consistency.

i. Calculated using scaling relation from ref. 10 and the OH adsorption enthalpy.

j. As no data is available for CH_3OO, the data of OOH is used as an approximation.

k. Adsorption of COOH and HCOO are only included in the simulations that investigate the effect of these particular species.

l. These reactions are only included when explicitly mentioned and their enthalpy barriers are varied during the simulation.

As indicated in Table S1, we combine the data for O_2 adsorption and O_2* dissociation from ref. 2 into one dissociative adsorption reaction, as this is more convenient for the implementation of O_2 vibrational excitation. The limit for lowering the Gibbs free energy barrier of this combined reaction due to vibrational excitation is set to 0.56 eV, which is the enthalpy barrier for dissociation of adsorbed O_2* reported in ref. 2. Thus, the Gibbs free energy is reduced by αE_v if $\alpha E_v < 0.56$ eV or by 0.56 eV if $\alpha E_v \geq 0.56$ eV. The value of the Fridman-Macheret α parameter (see next section) is calculated using the forward $(0.56\ \text{eV})^2$ and reverse $(1.82\ \text{eV})^2$ barriers for the dissociation of adsorbed O_2* (i.e. $\alpha = 0.24$). If the calculated Gibbs free energy barrier is smaller than the barrier for O_2 adsorption (corresponding to the loss of 1/3 of the translational entropy), the latter is used instead. This is done in order to make sure there is always a non-zero barrier for this process. Using the approximations above, O_2 is assumed to either immediately dissociate after adsorption, before thermalisation of T_{vib} with the surface can occur, or to desorb back to the gas phase.

2. The effect of vibrational excitation

The effect of vibrationally excited CH_4 and O_2 is accounted for by modifying the enthalpy barrier of their dissociative adsorption processes and the Eley-Rideal reactions between gaseous CH_4 and surface-bound OH* or O* (see Table S1, reactions 14 and 15). The forward rate constant of a reaction starting from a vibrationally excited CH_4 or O_2 molecule with vibrational level ν is calculated according to:[13]

$$k_{f,\nu} = \frac{k_b T}{h} \exp\left(\frac{\Delta S^{\ddagger}}{R}\right) \exp\left(-\frac{\Delta H^{\ddagger} - \alpha E_\nu}{RT}\right) = k_f \exp\left(\frac{\alpha E_\nu}{RT}\right) \qquad if\ \Delta H^{\ddagger} > \alpha E_\nu \quad (S1)$$

$$k_{f,\nu} = \frac{k_b T}{h} \exp\left(\frac{\Delta S^{\ddagger}}{R}\right) = k_f \exp\left(\frac{\Delta H^{\ddagger}}{RT}\right) \qquad if\ \Delta H^{\ddagger} \leq \alpha E_\nu \quad (S2)$$

Where E_ν is the energy of the vibrational level ν and α is the parameter of the Fridman-Macheret model, which denotes how efficiently the energy of a certain vibrational excitation can lower the energy barrier:[14]

$$\alpha = \frac{\Delta H_f^{\ddagger}}{\Delta H_f^{\ddagger} + \Delta H_r^{\ddagger}} \qquad (S3)$$

The Fridman-Macheret model is supported by the high efficiency factors that are observed for strong endothermic reactions, whose activation barriers are close to the reaction enthalpy, and the low efficiency factors associated with strong exothermic reactions, which generally have low activation barriers.[14]

The energy levels of the vibrational overtones are estimated using the harmonic approximation. For CH_4 only the symmetric (ν_1) and asymmetric (ν_3) stretch modes are considered, as the bending modes (ν_2 and ν_4) are less effective in breaking the C-H bond.[15] Additionally, we assume that the dissociation barrier is influenced by the total energy $E_{v,stretch}$ allocated in all stretch modes, i.e. we use $E_\nu = E_{v,stretch}$ in eqs S1 and S2. The population of the vibrational levels is assumed to follow a Boltzmann distribution:[15,16]

$$P(\nu) = \frac{g(\nu) \cdot \exp\left(\frac{-E_\nu}{k_b T_{vib}}\right)}{\sum_{\nu'=0}^{\nu_{max}} g(\nu') \cdot \exp\left(\frac{-E_{\nu'}}{k_b T_{vib}}\right)} \qquad (S4)$$

Where $P(\nu)$ is the fractional population of a vibrational level ν with energy E_ν and degeneracy $g(\nu)$ at a vibrational temperature T_{vib}. The denominator gives the total partition sum over all

levels that are considered, i.e. from the ground level to ν_{max}. For O_2, which has only one vibrational mode, the level degeneracy $g(v)$ is always equal to one and E_v is equal to the energy of the vibrational state. However, the situation is more complicated for CH_4 which has one symmetric stretch (ν_1), two doubly degenerate bending (ν_2), three triply asymmetric stretch (ν_3) and three triply degenerate bending modes (ν_4). The population of a vibrational state (ν_1, ν_2, ν_3, ν_4) for which the vibrational quantum numbers v_i of the four fundamental modes are specified can be calculated as described by Butterworth *et al.*:[16]

$$P(\nu_1, \nu_2, \nu_3, \nu_4) = \prod_{i=1,2,3,4} \frac{g_i(\nu_i) \cdot \exp\left(\frac{E_i}{k_b T_{vib}}\right)}{Q_i(T_{vib})} \qquad (S5)$$

Where $g_i(v_i)$ is the level degeneracy per mode, E_i is the level energy per mode and $Q_i(T_{vib})$ is the mode partition sum. As discussed above, we make the approximation that the dissociation barrier is affected by the total energy allocated to the stretch modes of a given vibrational state, but not by the energy allocated to the bending modes. Under these conditions, all vibrational states (ν_1, ν_2, ν_3, ν_4) for which $\nu_1 + \nu_3 = \nu_{stretch}$ and $\nu_2, \nu_4 \in [0, +\infty[$ experience the same modified rate constant for dissociation (see eqs S1 and S2). Additionally, the frequencies of the symmetric (ν_1) and asymmetric (ν_3) stretch modes are relatively close (2916 cm^{-1} and 3019 cm^{-1}, respectively).[15] Therefore, we treat the one ν_1 and the three ν_3 modes as four modes with the same vibrational frequency.[16] This frequency is set equal to the weighted average of the vibrational frequencies of these modes (2993 cm^{-1}). The combined population density $P_{comb}(v_{stretch})$ for all states which experience the same modified rate constant is then calculated as:

$$P_{comb}(\nu_{stretch}) = \frac{g_{stretch}(\nu_{stretch}) \cdot \exp\left(\frac{-E_{v,stretch}}{k_b T_{vib}}\right)}{\sum_{\nu'_{stretch}=0}^{\nu_{max}} g_{stretch}(\nu'_{stretch}) \cdot \exp\left(\frac{-E_{v',stretch}}{k_b T_{vib}}\right)} \qquad (S6)$$

Where $g_{stretch}(v_{stretch})$ is the level degeneracy for the stretch modes when these are considered together and $E_{v,stretch}$ is the total energy allocated in the stretch modes. We calculate $g_{stretch}(v_{stretch})$ as the number of ways that $v_{stretch}$ number of vibrational quanta can be distributed over the four stretch modes:

$$g_{stretch}(\nu_{stretch}) = \binom{3 + \nu_{stretch}}{\nu_{stretch}} = \frac{(3 + \nu_{stretch})!}{\nu_{stretch}!\, 3!} \qquad (S7)$$

From the modified rate constant and the populations, the total modified forward rate constant k_f' for all vibrational levels is calculated as:

$$k_f' = \sum_{v} k_{f,v} P(v) \qquad (S8)$$

With $v = v_{stretch}$ and $P(v) = P_{comb}(v_{stretch})$ in the case of CH_4.

Because the harmonic approximation does not account for the decrease in energy difference between vibrational levels upon increasing level, we use a cut-off for the number of levels included in the model. For CH_4, the first 12 vibrationally excited levels are included (v_{max} = 12), as the 12th level has an energy roughly equal to the C-H bond energy in CH_4. In the case of O_2, the first 26 vibrationally excited levels are considered (v_{max} = 26), as the energy of the 26th level is closest to the bond energy in O_2.

3. Turnover frequency (TOF) and selectivity

To compare the product formation and product distributions between different conditions, we calculate the steady state TOFs and selectivities. The steady state TOF of a gas species x_g is calculated as:

$$TOF(x_g) = \sum_{i,gain} c_{x_g,i} r_i - \sum_{i,loss} c_{x_g,i} r_i \qquad (S9)$$

Where c_{xg} is the stoichiometric coefficient of gas phase species x_g in reaction i, and r_i are the rates at steady state. The selectivity of a carbon-containing product $x_{g,C}$ is calculated as the percentage of the total sum of the TOFs of all formed carbon-containing products, taking into account the number of carbon atoms in each product species (n_x):

$$Selectivity(x_{g,C}) = \frac{n_x \times TOF(x_{g,C})}{\sum_{x_{g,C},TOF>0} n_x \times TOF(x_{g,c})} \times 100\% \qquad (S10)$$

4. Comparison of the thermal-catalytic pathways with literature

Figure 1a in the main paper describes the overall reaction pathways towards the main products for thermal-catalytic POX of CH_4 at 500 K using a 70/30 CH_4/O_2 mixture. These calculations are performed at 500 K, so that the results can serve as a benchmark for the plasma cases, which are simulated at conditions relevant for a DBD. In this section, we compare the reaction pathways from Figure 1a (see main paper) to pathways calculated for a temperature that is

relevant for thermal-catalytic POX of CH_4, i.e. 1000 K. These pathways are displayed in Figure S1. Additionally, we also compare our results to earlier microkinetic studies by Aghalayam *et al.*[17] and Mhadeshwar *et al.*[9] The results of Aghalayam *et al.* are calculated at 800 K and for a mixture of 10% CH_4 in air.[17] Those of Mhadeshwar *et al.* are calculated at 1123 K and for a mixture of 2% CH_4, 1.8% O_2 and 96.2% N_2.[9]

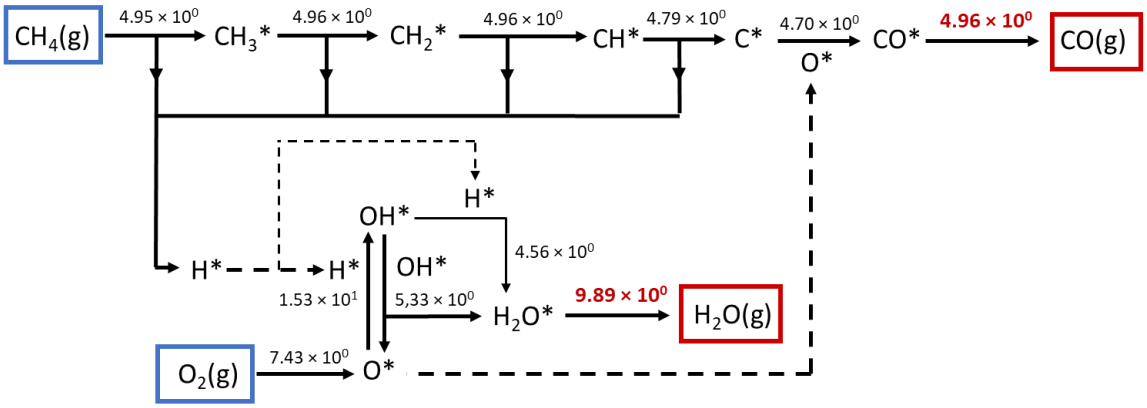

Figure S1. Most important reaction pathways at steady state for thermal-catalytic POX of CH_4 on Pt(111) using a CH_4/O_2 (70/30) gas mixture at 1000 K and 1 bar. The values of the reaction TOFs in (s^{-1}) are displayed next to the arrows. The arrow thickness indicates the relative importance of a reaction. A dotted arrow indicates the species is used as a second reactant in another reaction.

The reaction pathways at 500 K (Figure 1a in the main paper) and at 1000 K (Figure S1) are largely similar. Under both conditions, the activation of CH_4 occurs through dissociative adsorption on empty sites, followed by dehydrogenation of CH_3* and CH_2* by empty surface sites. In contrast, the models by Aghalayam *et al.*[17] and Mhadeshwar *et al.*[9] predict that CH_x* dehydrogenation occurs mainly via an O*-assisted route. However, these models are based on the less accurate bond order conservation theory, which predicts lower activation barriers for the O*-assisted route, while various DFT studies found that for Pt the O*-assisted route has higher barriers.[7,18,19] At 1000 K, CH* is dehydrogenated through interaction with an empty site and the formed C* is subsequently oxidised to CO*. Aghalayam *et al.*[17] and Mhadeshwar *et al.*[9] instead reported that CH* mainly reacts with O* to form CO* and H* via a direct route. At 500 K, we find that CH* dissociation and subsequent C* oxidation is only a secondary route, as CH* mainly (90.5%) reacts with O* to form CHO*. This is likely a result of the higher O* coverage at this temperature. The formed CHO* subsequently decomposes to CO* and H*. Note that this route is similar to the one reported by Aghalayam *et al.*[17] and Mhadeshwar *et al.*[9] as the formation of CO* from CH* occurs through interaction between CH* and O* and does not go via C*. Aghalayam *et al.*[17] and Mhadeshwar *et al.*[9] both reported that CO* is further oxidised to CO_2*. As is discussed in the next section, we find that the importance of this reaction

depends on the presence of small amounts of CO in the gas phase and on the temperature. In accordance with Mhadeshwar *et al.*,[9] we find that H_2O^* is formed through disproportionation of two OH* species. Yet, at 1000 K, we find that the hydrogenation of OH* is only slightly less important (46.1%) for the formation of H_2O^* than the disproportionation of OH* species, which forms 53.8% of H_2O^*.

5. Effect of CO on CO_2 selectivity in thermal POX of CH_4

There exists a discussion in literature about whether syngas formation via POX of CH_4 in thermal catalysis occurs via a direct or an indirect mechanism. The direct mechanism claims that CO and H_2 are mainly formed directly from CH_4 and O_2. The indirect mechanism assumes that two zones are present in the reactor: an oxidation zone at the start of the reactor and a successive reforming zone. In the oxidation zone, O_2 is consumed in the total oxidation of CH_4, to primarily form CO_2 and H_2O. In the subsequent reforming zone, where O_2 has been depleted, the formed CO_2 and H_2O react with the remaining CH_4 via dry and steam reforming, respectively, to form syngas.[20] Based on whether a direct, indirect or intermediate mechanism occurs, we can thus expect either syngas, complete oxidation products or a mixture of both, as the main products in the presence of O_2. The more recent studies on thermal-catalytic POX of CH_4 on Pt seem to support either the indirect[9,17,21] or intermediate mechanism.[20,22,23] However, at the relatively low temperature of 500 K of our simulations, H_2O and CO_2 are the thermodynamically favoured products according to thermodynamic equilibrium calculations. We could thus expect the formation of CO_2 to be favoured over that of CO. The fact that our model does not predict this, however, can be attributed to the zero conversion conditions.

Figure S2 illustrates that the presence of small fractions of CO (0.1-0.001%) in a CH_4/O_2 gas mixture causes CO_2 to become the main product at temperatures below 1000 K. This shows that the formation of CO_2 in the thermal POX of CH_4 depends on the presence of small quantities of CO in the gas phase. High CO content and low temperature favour CO_2, while low CO content and high temperature favour CO. Note that other products, e.g. H_2, H_2O and CO_2, will also form and accumulate in the gas phase, which will further influence the selectivities towards CO and CO_2. In order to make more accurate predictions of which product is favoured under the different reaction conditions, a reactor model is required that considers the change in gas phase composition, based on product formation. However, this is outside the scope of the present study.

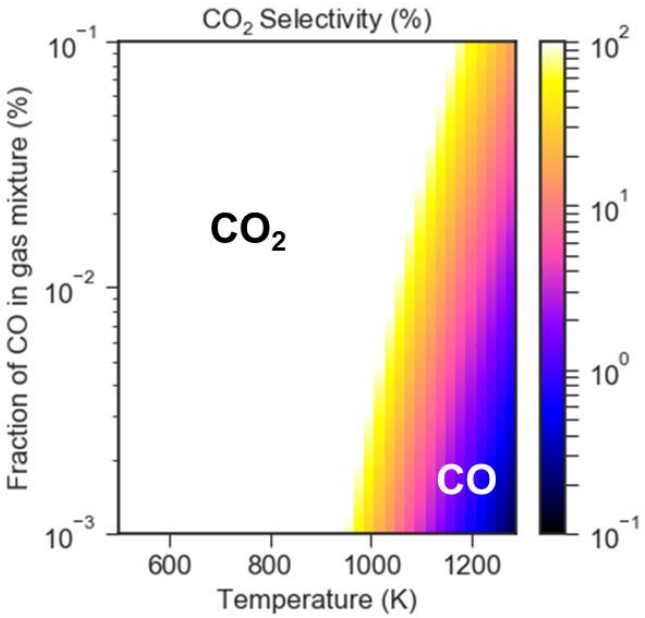

Figure S2. The influence of small fractions of CO in a CH_4/O_2 (70/30) gas mixture and of temperature on the CO_2 selectivity in (%) for thermal-catalytic POX of CH_4 on Pt(111). Calculated at steady-state and for a total pressure of 1 bar.

6. Influence of vibrational excitation on the surface coverages

Figure S3 shows the surface coverages of the 14 most abundant surface species, as well of the fraction of free sites, when varying the vibrational temperature between 500 and 1500 K and the O_2 content between 1 and 99%. O* species cover almost the whole surface for the entire range of investigated conditions, but its coverage decreases slightly when lowering the O_2 content or increasing the vibrational temperature. The fraction of free sites mainly depends on the O_2 content in the gas mixture and increases upon decreasing O_2 fraction. The coverages of the other species increase with rising vibrational temperature, while many also show some dependency on the O_2 fraction.

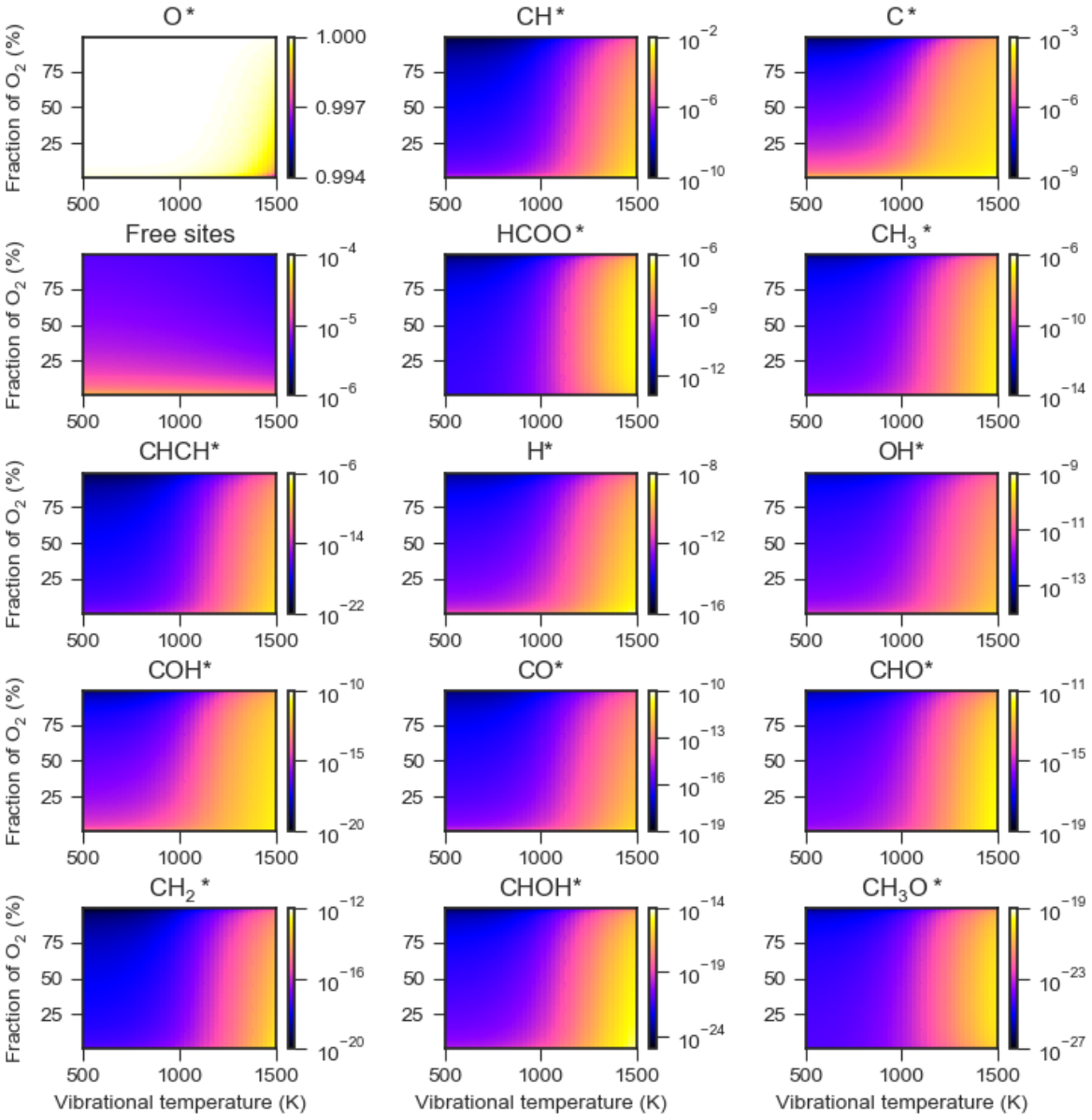

Figure S3. Influence of the vibrational temperature and O_2 content on the fractional coverages of the 14 most abundant surface species, as well as the fraction of free sites. Calculated at steady state for a CH_4/O_2 mixture at a pressure of 1 bar and a surface temperature of 500 K. Note that linear scaling is used for the O coverage, while logarithmic scaling is used for the other surface coverages.*

7. Influence of vibrational excitation on the selectivities of CH_2CH_2 and CHCH

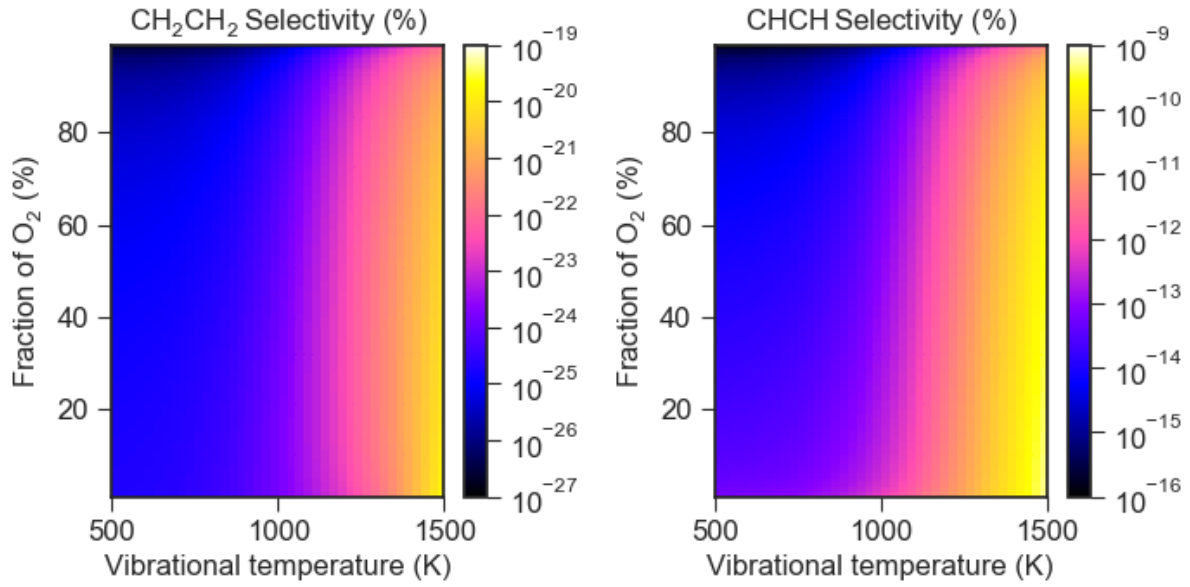

Figure S4. Influence of the vibrational temperature and O_2 content on the selectivities of CH_2CH_2 and CHCH. Calculated at steady state for a CH_4/O_2 mixture at a pressure of 1 bar and a surface temperature of 500 K.

8. Effect of vibrational excitation in the presence of radicals

Figure S5 illustrates the effect of the vibrational temperature of CH_4 and O_2 on the TOFs of the products and reactants, when radicals are present in the gas phase. All TOFs, except that of CH_4 dissociation, remain constant as the vibrational temperature rises from 500 to 1500 K. This indicates that in the presence of radicals, vibrational excitation of CH_4 and O_2 has only a negligible effect on the surface chemistry, and consequently that the surface chemistry is mainly governed by the plasma radicals. While the TOF of CH_4 dissociation does change when the vibrational temperature rises above 1000 K, this does not affect the TOFs of any other reactants or products. Below 1160 K, CH_4 is net formed at the surface, as its dissociation products from the plasma, i.e. CH_3 and H, adsorb onto the surface and recombine to form CH_4. At higher temperatures, the dissociation of vibrationally excited CH_4 becomes more important, resulting in a net consumption of CH_4 at the surface. Note that the CH_4 dissociation TOFs at the catalyst surface are low for these conditions. Therefore, CH_4 conversion will mainly occur in the plasma, resulting in the formation of reactive radicals that react much faster at the surface.

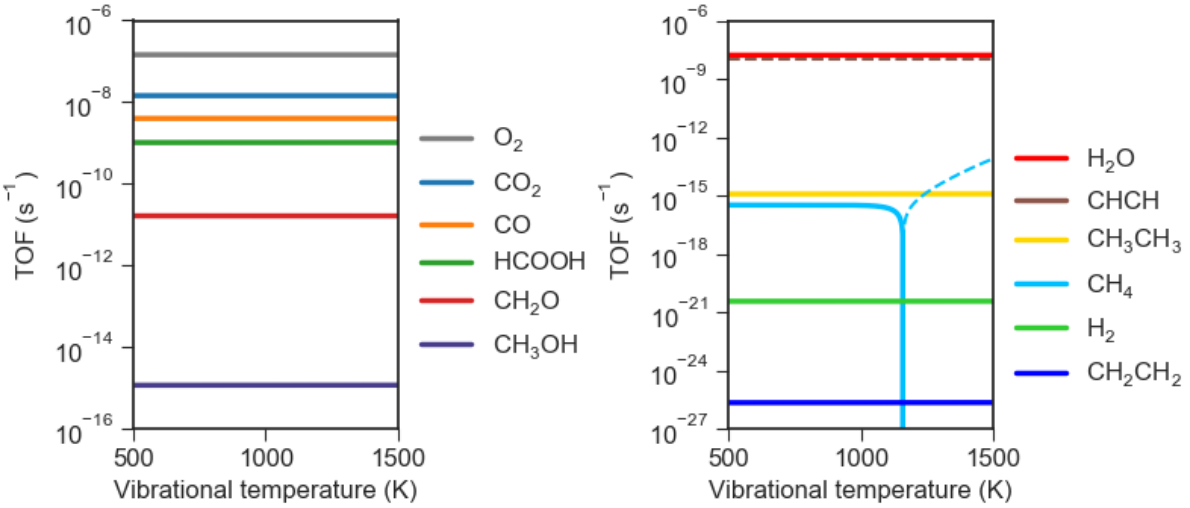

Figure S5. Effect of the vibrational temperature on the TOFs of products and reactants when radicals are present in the gas phase. Dotted lines indicate consumption, whereas full lines indicate production. Calculated for a surface temperature of 500 K and a total pressure of 1 bar. The partial pressures used in the simulations are shown Table 1 of the main paper.

9. Effect of OH and OOH radicals on TOFs and surface coverages

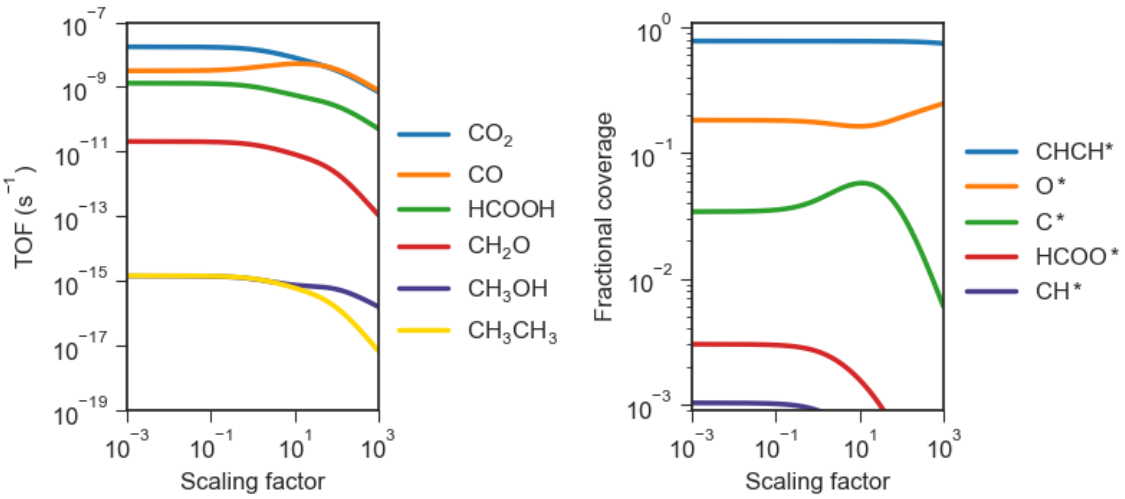

Figure S6. Influence of the OH and OOH partial pressures on TOFs (left) and surface coverages (right). Calculated for a surface temperature of 500 K and a total pressure of 1 bar. The species partial pressures used in the simulations are shown in Table 1 of the main paper, but the partial pressures of OH and OOH are varied by the indicated scaling factor.

10. Effect of HCOO and COOH radicals on TOFs and surface coverages

As mentioned before, we estimated the partial pressures of the various plasma species based on the densities calculated by De Bie *et al.*[24] (see Table 1 of the main paper). However, the model by De Bie *et al.* does not include HCOO and COOH radicals. Yet, these species might also have an important influence on the surface chemistry. In this section, we therefore briefly discuss their potential effect. To investigate this, we include the adsorption and desorption of

these species in the chemistry set and choose a low value of 10^{-13} bar for their partial pressures, so that these radicals do not influence the rest of the surface chemistry. We then separately increase their partial pressures by up to a factor 10^{6}, i.e. up to a maximum partial pressure of 10^{-7} bar. The resulting variations in TOFs and surface coverages are displayed in Figure S7 and Figure S8 for HCOO and COOH, respectively. Enhanced adsorption of HCOO leads to a higher formation of CO_2 and HCOOH, according to the pathways in Figure 4 of the main paper. The higher CO_2* formation enhances CO production via the reverse Boudouard reaction, while the higher consumption of H* upon hydrogenation of HCOO* hampers CH_3OH formation. A higher partial pressure of COOH also favours the production of CO_2 through hydrogen abstraction from the adsorbed COOH* by O*. This also leads to a higher TOF of CO, caused by the reverse Boudouard reaction. Thus, HCOO and COOH radicals mainly result in additional formation of unwanted CO_2 and CO, and their formation in the plasma should therefore be limited. On the other hand, the formation of HCOO in the plasma might be beneficial if HCOOH is the desired product.

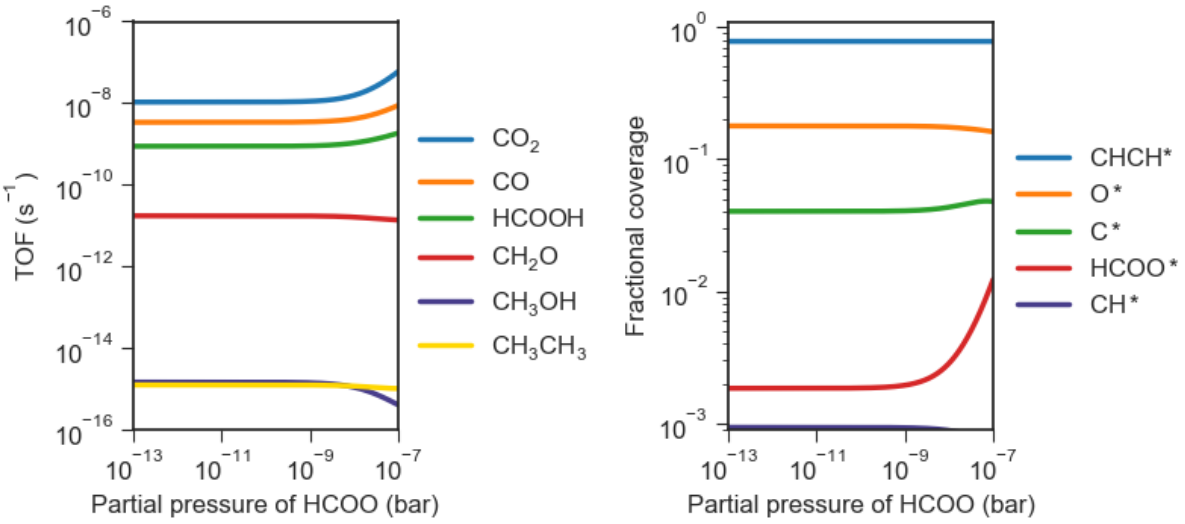

Figure S7. Influence of the HCOO partial pressure on TOFs (left) and surface coverages (right). Calculated for a surface temperature of 500 K and a total pressure of 1 bar. The partial pressure of HCOO is varied throughout the simulation, the partial pressure of COOH is kept constant at 10^{-13} bar, and the other partial pressures are shown Table 1 of the main paper.

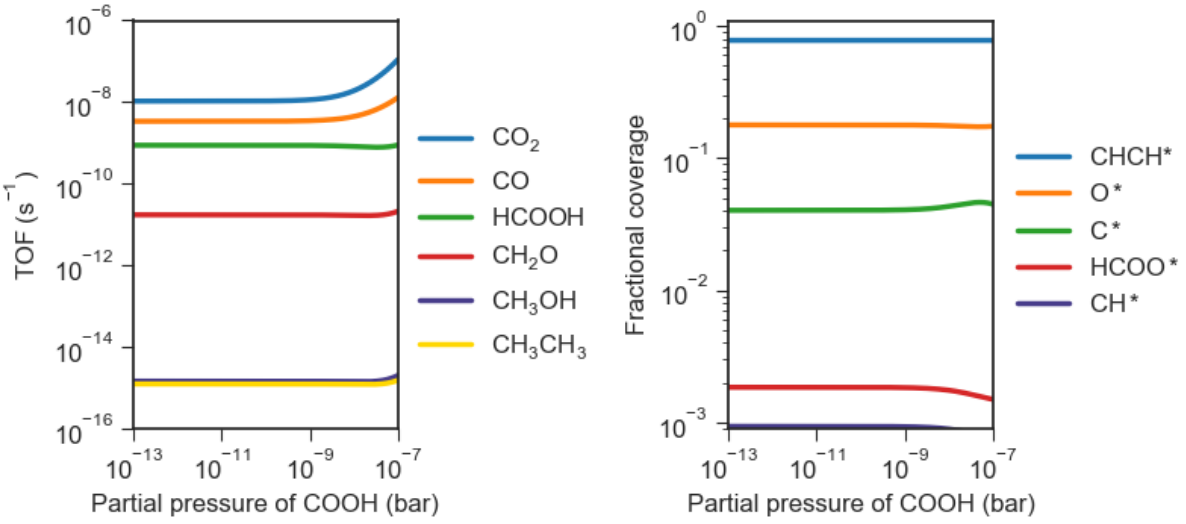

Figure S8. Influence of the COOH partial pressure on TOFs (left) and surface coverages (right). Calculated for a surface temperature of 500 K and a total pressure of 1 bar. The partial pressure of COOH is varied throughout the simulation, the partial pressure of HCOO is kept constant at 10^{-13} bar, and the other partial pressures are shown Table 1 of the main paper.

References

(1) Chen, Y.; Vlachos, D. G. Hydrogenation of Ethylene and Dehydrogenation and Hydrogenolysis of Ethane on Pt(111) and Pt(211): A Density Functional Theory Study. *J. Phys. Chem. C* **2010**, *114*, 4973–4982.

(2) Yang, Z.; Wang, J.; Yu, X. Density Functional Theory Studies on the Adsorption, Diffusion and Dissociation of O_2 on Pt(111). *Phys. Lett. A* **2010**, *374*, 4713–4717.

(3) Sutton, J. E.; Vlachos, D. G. Effect of Errors in Linear Scaling Relations and Brønsted–Evans–Polanyi Relations on Activity and Selectivity Maps. *J. Catal.* **2016**, *338*, 273–283.

(4) Yoo, J. S.; Abild-Pedersen, F.; Nørskov, J. K.; Studt, F. Theoretical Analysis of Transition-Metal Catalysts for Formic Acid Decomposition. *ACS Catal.* **2014**, *4*, 1226–1233.

(5) Wellendorff, J.; Silbaugh, T. L.; Garcia-Pintos, D.; Nørskov, J. K.; Bligaard, T.; Studt, F.; Campbell, C. T. A Benchmark Database for Adsorption Bond Energies to Transition Metal Surfaces and Comparison to Selected DFT Functionals. *Surf. Sci.* **2015**, *640*, 36–44.

(6) Stamatakis, M.; Chen, Y.; Vlachos, D. G. First-Principles-Based Kinetic Monte Carlo Simulation of the Structure Sensitivity of the Water–Gas Shift Reaction on Platinum

Surfaces. *J. Phys. Chem. C* **2011**, *115*, 24750–24762.

(7) Chen, Y.; Vlachos, D. G. Density Functional Theory Study of Methane Oxidation and Reforming on Pt(111) and Pt(211). *Ind. Eng. Chem. Res.* **2012**, *51*, 12244−12252.

(8) Greeley, J.; Mavrikakis, M. A First-Principles Study of Methanol Decomposition on Pt(111). *J. Am. Chem. Soc.* **2002**, *124*, 7193–7201.

(9) Mhadeshwar, A. B.; Vlachos, D. G. A Catalytic Reaction Mechanism for Methane Partial Oxidation at Short Contact Times, Reforming, and Combustion, and for Oxygenate Decomposition and Oxidation on Platinum. *Ind. Eng. Chem. Res.* **2007**, *46*, 5310–5324.

(10) Calle-Vallejo, F.; Loffreda, D.; Koper, M. T. M.; Sautet, P. Introducing Structural Sensitivity into Adsorption–Energy Scaling Relations by Means of Coordination Numbers. *Nat. Chem.* **2015**, *7*, 403–410.

(11) Yu, T. H.; Hofmann, T.; Sha, Y.; Merinov, B. V.; Myers, D. J.; Heske, C.; Goddard, W. A. Finding Correlations of the Oxygen Reduction Reaction Activity of Transition Metal Catalysts with Parameters Obtained from Quantum Mechanics. *J. Phys. Chem. C* **2013**, *117*, 26598–26607.

(12) Todorovic, R.; Meyer, R. J. A Comparative Density Functional Theory Study of the Direct Synthesis of H_2O_2 on Pd, Pt and Au Surfaces. *Catal. Today* **2011**, *160*, 242–248.

(13) Engelmann, Y.; Mehta, P.; Neyts, E. C.; Schneider, W. F.; Bogaerts, A. Predicted Influence of Plasma Activation on Nonoxidative Coupling of Methane on Transition Metal Catalysts. *ACS Sustain. Chem. Eng.* **2020**, *8*, 6043–6054.

(14) Fridman, A. *Plasma Chemistry*; Cambridge University Press: New York, 2008.

(15) Juurlink, L. B. F.; Killelea, D. R.; Utz, A. L. State-Resolved Probes of Methane Dissociation Dynamics. *Prog. Surf. Sci.* **2009**, *84*, 69–134.

(16) Butterworth, T.; van de Steeg, A.; van den Bekerom, D.; Minea, T.; Righart, T.; Ong, Q.; van Rooij, G. Plasma Induced Vibrational Excitation of CH_4 —a Window to Its Mode Selective Processing. *Plasma Sources Sci. Technol.* **2020**, *29*, 095007.

(17) Aghalayam, P.; Park, Y. K.; Fernandes, N.; Papavassiliou, V.; Mhadeshwar, A. B.; Vlachos, D. G. A C1 Mechanism for Methane Oxidation on Platinum. *J. Catal.* **2003**, *213*, 23–38.

(18) Yoo, J. S.; Khan, T. S.; Abild-Pedersen, F.; Nørskov, J. K.; Studt, F. On the Role of the Surface Oxygen Species during A–H (A = C, N, O) Bond Activation: A Density Functional Theory Study. *Chem. Commun.* **2015**, *51*, 2621–2624.

(19) Xing, B.; Pang, X.-Y.; Wang, G.-C. C–H Bond Activation of Methane on Clean and Oxygen Pre-Covered Metals: A Systematic Theoretical Study. *J. Catal.* **2011**, *282*, 74–82.

(20) Horn, R.; Williams, K.; Degenstein, N.; Bitsch-Larsen, A.; Dalle Nogare, D.; Tupy, S.; Schmidt, L. Methane Catalytic Partial Oxidation on Autothermal Rh and Pt Foam Catalysts: Oxidation and Reforming Zones, Transport Effects, and Approach to Thermodynamic Equilibrium. *J. Catal.* **2007**, *249*, 380–393.

(21) Chin, Y.-H. C.; Buda, C.; Neurock, M.; Iglesia, E. Selectivity of Chemisorbed Oxygen in C–H Bond Activation and CO Oxidation and Kinetic Consequences for CH_4–O_2 Catalysis on Pt and Rh Clusters. *J. Catal.* **2011**, *283*, 10–24.

(22) Korup, O.; Goldsmith, C. F.; Weinberg, G.; Geske, M.; Kandemir, T.; Schlögl, R.; Horn, R. Catalytic Partial Oxidation of Methane on Platinum Investigated by Spatial Reactor Profiles, Spatially Resolved Spectroscopy, and Microkinetic Modeling. *J. Catal.* **2013**, *297*, 1–16.

(23) Bitsch-Larsen, A.; Horn, R.; Schmidt, L. D. Catalytic Partial Oxidation of Methane on Rhodium and Platinum: Spatial Profiles at Elevated Pressure. *Appl. Catal. A* **2008**, *348*, 165–172.

(24) De Bie, C.; van Dijk, J.; Bogaerts, A. The Dominant Pathways for the Conversion of Methane into Oxygenates and Syngas in an Atmospheric Pressure Dielectric Barrier Discharge. *J. Phys. Chem. C* **2015**, *119*, 22331–22350.